RESEARCH ARTICLE
SPACE PHYSICS: IONOSPHERIC PHYSICS

Earth and Planetary Physics
7: 378–388, 2023
doi: 10.26464/epp2023037

Solar cycle variations in equatorial ionospheric zonal electric fields near sunrise

JunJie Chen[1,2,3], WenBin Wang[4], JiuHou Lei[1*], and Tong Dang[1]

[1]Space Exploration Laboratory/School of Earth and Space Sciences, University of Science and Technology of China, Hefei 230026, China;

[2]Department of Earth Sciences, The University of Hong Kong, Pokfulam, Hong Kong SAR, China;

[3]Chinese Academy of Sciences (CAS) Center for Excellence in Comparative Planetology/CAS Key Laboratory of Geospace Environment/Mengcheng National Geophysical Observatory, University of Science and Technology of China, Hefei 230026, China;

[4]High Altitude Observatory, National Center for Atmospheric Research, Boulder, CO 80307, USA

Key Points:

- The equatorial eastward electric fields near sunrise decrease with an increase in solar activity regardless of the longitude and season.
- This solar cycle dependence is related to the F-region dynamo resulting from the stronger responses of conductivity and zonal winds in the F-region.
- As solar activity increases, the F-region zonal wind dynamo produces westward electric fields at sunrise to offset the sunrise enhancement induced by the E-region dynamo.

Citation: Chen, J. J., Wang, W. B., Lei, J. H., and Dang, T. (2023). Solar cycle variations in equatorial ionospheric zonal electric fields near sunrise. *Earth Planet. Phys.*, *7*(3), 378–388. http://doi.org/10.26464/epp2023037

Abstract: In this study, we investigate the solar cycle dependence of the sunrise ionospheric zonal electric fields at the equator under geomagnetically quiet conditions. Simulations using the Thermosphere–Ionosphere–Electrodynamics General Circulation Model (TIEGCM) reveal that the equatorial eastward electric field at sunrise decreases with the increase in solar activity, independent of longitude, season, and lower atmospheric tides. The solar cycle dependence of the sunrise zonal electric field is mainly related to the zonal wind dynamo. Moreover, this solar cycle dependence of sunrise electric fields at the equator is dominated by the corresponding variation in the F-region dynamo because the response of conductivity and neutral winds near sunrise to increasing solar flux is stronger in the F-region than in the E-region, although the sunrise eastward enhancement of electric fields is mainly driven by the E-region zonal wind dynamo. Specifically, the westward gradient of low-latitude F-region neutral winds near the dawn terminator tends to produce westward electric fields in the equatorial region that are more pronounced at solar maximum, whereas the midlatitude E-region dynamo induces an eastward enhancement of sunrise electric fields at the equator that decreases slightly with increasing solar activity. This study also reveals that the reason the eastward enhancement of equatorial zonal electric fields near dawn and dusk terminators show opposite solar cycle dependence is because of their different generation mechanisms.

Keywords: ionosphere; electrodynamics; sunrise enhancement; solar cycle dependence

1. Introduction

Solar radiation plays a significant role in the coupled thermosphere–ionosphere system of the Earth. An enhancement in solar extreme ultraviolet (EUV) radiation increases the daytime ion production (Rishbeth and Garriott, 1969) and the ionospheric plasma density (Wright, 1962; De Adler et al., 1997; Richards, 2001), which enhances Pedersen and Hall conductivities (e.g., Baker and Martyn, 1953; Kelley, 2009). The change in solar EUV radiation also alters the heat input to the terrestrial thermosphere and causes variations in neutral density and temperature (Hagan and Oliver, 1985; Hedin and Mayr, 1987, and references therein). These variations then change both the neutral pressure gradient and the ion drag to affect the neutral wind velocity in the geographic height coordinates. Furthermore, solar cycle variations in ionospheric conductivity and thermosphere winds (Hedin et al., 1994; Drob et al., 2015) induce corresponding changes in the dynamo electric fields (Fejer et al., 1979, 1991, 2008) by ionospheric electrodynamics (Richmond, 1995a; Heelis, 2004).

Although the understanding of ionospheric zonal electric fields near sunrise has improved over the past three decades, these electric fields have not received as much attention as those at other local times (LTs) because long-term averaged observational results near 6:00 LT are complicated by the transition between the nighttime westward and daytime eastward electric fields (Fejer et al., 1979, 1991, 2008; Kil et al., 2009). Recently, increased attention has been given to the sunrise eastward enhancement of

First author: J. J. Chen, cjjvince@hku.hk
Correspondence to: J. H. Lei, leijh@ustc.edu.cn
Received 22 DEC 2022; Accepted 01 APR 2023.
Accepted article online 14 APR 2023.

zonal electric fields with a magnitude of 0.5–2.0 mV/m between 4:00 and 8:00 LT, in the form of case studies (Aggson et al., 1995; Kelley et al., 2014; Zhang RL et al., 2016), statistical analyses (Zhang RL et al., 2015), and numerical simulations (Liu HL and Richmond, 2013; Chen JJ et al., 2020, 2021b).

Observations by the Republic of China Satellite 1 (ROCSAT-1) indicate that long-term average sunrise equatorial electric fields become more westward at solar maximum under most longitudinal and seasonal conditions (Fejer et al., 2008; Kil et al., 2009). However, these long-term average results tend to smooth out the sunrise eastward enhancement, although its frequency of occurrence was reported as approximately 30% in a statistical study based on the same data (Zhang RL et al., 2015). Hence, the solar cycle variation in the sunrise enhancement needs further study. Simulation studies have shown that the magnitude of sunrise electric fields, as well as the equatorial sunrise enhancement, actually decreases with increasing solar activity when driven by lower atmospheric tides (Liu HL and Richmond, 2013; Fang TW et al., 2014). However, these simulations have not taken into account the solar cycle variation of the sunrise electric fields for different longitudinal, seasonal, and tidal conditions. In addition, physical processes contributing to the solar cycle dependence of sunrise electric fields have never been quantitatively assessed.

The Thermosphere–Ionosphere–Electrodynamics General Circulation Model (TIEGCM) is a first-principles, time-dependent, three-dimensional model of the coupled thermosphere–ionosphere system (Roble et al., 1988; Richmond et al., 1992) that enables studies of the sunrise eastward enhancement of zonal electric fields. The TIEGCM was able to reproduce a strong sunrise enhancement event observed by the Jicamarca incoherent scatter radar near the June solstice at solar minimum (Chen JJ et al., 2020). That study also revealed that the midlatitude E-region dynamo could be a major source of equatorial sunrise enhancement. The TIEGCM-simulated longitudinal variation in the sunrise enhancement is also generally consistent with the ROCSAT-1 observations (Zhang RL et al., 2015; Chen JJ et al., 2021b). Therefore, the TIEGCM is an effective tool to further explore the solar cycle variation in the sunrise electric fields and its associated physical mechanisms.

In this study, we first compare the solar cycle variation in quiet-time zonal electric fields near sunrise under different seasonal, longitudinal, and tidal conditions. We then utilize a controlled-variable method to analyze the solar cycle variation in electric fields driven by different wind dynamo sources. Finally, we diagnostically analyze in detail the effect of solar cycle changes in neutral winds and conductivity at different altitudes on the sunrise electric field variation.

2. Methodology

This study uses the TIEGCM version 2.0, which has a horizontal resolution of 2.5° × 2.5° in geographic longitude and latitude and a vertical resolution of 1/4 scale height in pressure surface. The pressure surface is defined as $\ln(p_0/p)$ ranging from −7 to 7, where p is neutral pressure and p_0 is a reference pressure of 5×10^{-7} hPa. The lower boundary is approximately 97 km and the upper boundary is approximately 450–700 km, depending on solar activity. The lower boundary atmospheric tides were provided by the empirical Global Scale Wave Model (Hagan and Forbes, 2002, 2003). The cross-polar cap potential was set to 0 to eliminate the impacts of ionospheric convection patterns at high latitudes.

Without high-latitude convection, the equatorial ionospheric electric potentials and electric fields were determined by the E- and F-region neutral wind dynamos (Richmond, 1995a; Chen JJ and Lei JH, 2019). Electric potentials were calculated in a dynamo module by solving the electrodynamics equation assuming divergence-free currents ($\nabla\cdot\boldsymbol{J}=0$) (Richmond, 1995b; Richmond and Maute, 2014). The polarization electric field ($\boldsymbol{E}$) and total current density ($\boldsymbol{J}$) in the ionosphere can be expressed as follows:

$$\boldsymbol{E}=-\nabla\Phi, \tag{1}$$

$$\boldsymbol{J}=\sigma_P(\boldsymbol{E}+\boldsymbol{U}\times\boldsymbol{B})+\sigma_H\boldsymbol{b}\times(\boldsymbol{E}+\boldsymbol{U}\times\boldsymbol{B}), \tag{2}$$

where Φ is the electric potential that is assumed to be equal along the geomagnetic field line; $\boldsymbol{b}$ is the unit vector parallel to the geomagnetic field $\boldsymbol{B}$; σ_P and σ_H are the Pedersen and Hall conductivities; and $\boldsymbol{U}$ is the horizontal neutral wind on a constant pressure surface. The TIEGCM-simulated neutral winds were generally consistent with observations (Lei JH et al., 2007; Luan XL and Solomon, 2008; Jiang GY et al., 2018), which was essential to isolate the contribution of the wind dynamo to the electric fields. Finally, the electric potential was obtained by solving the electrodynamics equation expressed by

$$\nabla\cdot\int_S^N(\sigma_P\nabla\Phi+\sigma_H\boldsymbol{b}\times\nabla\Phi)\mathrm{d}s=\nabla\cdot\int_S^N[\sigma_P\boldsymbol{U}\times\boldsymbol{B}+\sigma_H\boldsymbol{b}\times(\boldsymbol{U}\times\boldsymbol{B})]\mathrm{d}s, \tag{3}$$

where the field-aligned integral is along geomagnetic field lines between southern (S) and northern (N) foot points at a 90 km altitude. The expression $\boldsymbol{U}\times\boldsymbol{B}$ includes eastward and poleward or upward components perpendicular to the geomagnetic field, namely, $(\boldsymbol{U}\times\boldsymbol{B})_{\perp x}$ and $(\boldsymbol{U}\times\boldsymbol{B})_{\perp y}$, where the subscripts x and y represent zonal and meridional directions. Here, $(\boldsymbol{U}\times\boldsymbol{B})_{\perp x}$ and $(\boldsymbol{U}\times\boldsymbol{B})_{\perp y}$ correspond to the dynamo effects of meridional (U_y) and zonal winds (U_x), respectively. The overall effect of the zonal wind dynamo from different altitudes on electric field generation can be roughly represented by the hemispheric height-integrated Pedersen conductivity-weighted $(\boldsymbol{U}\times\boldsymbol{B})_{\perp y}$, $(\boldsymbol{U}\times\boldsymbol{B})^P_{\perp y}$, defined as

$$(\boldsymbol{U}\times\boldsymbol{B})^P_{\perp y}=\int_{h_l}^{h_u}\sigma_P(\boldsymbol{U}\times\boldsymbol{B})_{\perp y}\mathrm{d}h/\Sigma_P, \tag{4}$$

$$\Sigma_P=\int_{h_l}^{h_u}\sigma_P\mathrm{d}h, \tag{5}$$

where the height integral is from the lower boundary (h_l) to the upper boundary (h_u); Σ_P is the hemispheric Pedersen conductance; and $(\boldsymbol{U}\times\boldsymbol{B})^P_{\perp y}$ is close to the value of $(\boldsymbol{U}\times\boldsymbol{B})_{\perp y}$ in the altitudinal range with high Pedersen conductivity, which is usually located in the E-region during the daytime and in the F-region at night (Heelis, 2004). Note that Hall conductivity always peaks in the E-region.

In this study, TIEGCM runs were conducted to investigate the solar cycle variation of the equatorial zonal electric field near sunrise and the relative contribution of different physical processes. First, three standard simulations were conducted with lower atmospheric tides specified at the lower boundary and different solar activity conditions ($F_{10.7}$ = 70, 130, and 200) to produce overall

solar cycle changes in the equatorial zonal electric field near sunrise. Three simulations were then run without tides at the lower boundary to analyze the tidal effects. The runs without tides at solar minimum ($F_{10.7}$ = 70) and maximum ($F_{10.7}$ = 200) are labeled F070STD and F200STD for reference in later analyses. To isolate the influence of different dynamo electric fields between solar minimum and solar maximum, a series of controlled numerical experiments were performed using a controlled-variable method developed in previous studies (Dang T et al., 2016; Chen JJ and Lei JH, 2019; Chen JJ et al., 2020).

Table 1 presents the detailed model settings for all controlled simulations. Electric fields in F070STD or F200STD were generated by the dynamo effects of both zonal and meridional winds. To compare solar cycle variations of the electric field driven by zonal and meridional wind dynamos, two controlled simulations (F070MW0 and F200MW0) were performed. In F070MW0 and F200MW0, meridional winds were set to 0 so that only the current generated by zonal winds was included in the dynamo module. Because the total dynamo electric fields in F070STD and F200STD were the linear summation of the dynamo effects of zonal and meridional winds, the difference between F070STD and F070MW0 (F200STD and F200MW0) gave the dynamo electric field driven only by the meridional wind dynamo at solar minimum (maximum). Additionally, F070ZWE0 and F200ZWE0 were conducted in a similar way to further isolate the effects of the zonal wind dynamo in the E-region and F-region. In F070ZWE0 and F200ZWE0, meridional winds and E-region zonal winds were set to 0 so that only the current generated by F-region zonal winds was included in the dynamo module. The difference between F070MW0 and F070ZWE0 (F200MW0 and F200ZWE0) gave the dynamo electric field driven only by the E-region zonal wind dynamo at solar minimum (maximum). Finally, we investigated in detail how solar cycle variations in conductivity and zonal winds at different altitudes cause the solar cycle dependence of the F-region zonal wind dynamo by running simulations based on F070ZWE0 with only retaining F-region zonal wind dynamo but replacing F-region conductivity (F070COFr) or E-region conductivity (F070COEr) or F-region zonal winds (F070ZWFr) at solar minimum with that from F200STD.

3. Results

3.1 The Solar Cycle Variation in Equatorial Zonal Electric Fields Near Sunrise

Figure 1 shows the temporal variations in equatorial zonal electric fields at the June solstice (day of year 173) at solar minimum and maximum with tidal effects. The June solstice is used as an example because the sunrise enhancement of equatorial zonal electric fields has a large occurrence rate and magnitude in observations (Zhang RL et al., 2015). The sunrise eastward enhancement in equatorial zonal electric fields lasts several hours, from 4:30 to 7:00 LT, at solar minimum. But the sunrise zonal electric field at solar maximum undergoes a transition between the nighttime westward and daytime eastward electric fields.

Figure 2 shows the solar cycle variation of the equatorial zonal electric fields at 6:00 LT under different longitudinal, seasonal, and tidal conditions. Figure 2a shows the longitudinal variation in the sunrise equatorial zonal electric field during the June solstice from three standard simulations, including tidal effects for $F_{10.7}$ = 70, 130, and 200. For all solar activity levels, the sunrise equatorial zonal electric field at the June solstice shows consistent longitudinal distributions with two maxima near 90°W and 115°E and two minima near 40°W and 160°E. When solar activity increases from $F_{10.7}$ = 70 to 200, the equatorial electric field at 6:00 magnetic local time (MLT) decreases at all longitudes. The electric field difference

Table 1. Control simulations to examine the solar activity dependence of equatorial sunrise zonal electric fields driven by different wind dynamo sources.

Run	Parameter setting	Purpose
1. F070STD	$F_{10.7}$ = 70	Solar minimum standard (STD) run
2. F200STD	$F_{10.7}$ = 200	Solar maximum standard run
3. F070MW0	$F_{10.7}$ = 70, without meridional winds (MW0)	Separate the effects of zonal and meridional wind dynamos at solar minimum
4. F200MW0	$F_{10.7}$ = 200, without meridional winds (MW0)	Separate the effects of zonal and meridional wind dynamos at solar maximum
5. F070ZWE0	$F_{10.7}$ = 70, without E-region zonal winds (ZWE0) at pressure level (Z_p) < −2 and meridional winds	Determine the F-region and E-region zonal wind dynamo effects at solar minimum
6. F200ZWE0	$F_{10.7}$ = 200, without E-region zonal winds at Z_p < −2 and meridional winds	Determine the F-region and E-region zonal wind dynamo effects at solar maximum
7. F070COFr	$F_{10.7}$ = 70, same as F070ZWE0 with only F-region zonal winds but replaced by F-region conductivity (COFr) at Z_p > −2 from F200STD	Isolate the effect of the solar cycle change in F-region conductivity on the F-region zonal wind dynamo
8. F070COEr	$F_{10.7}$ = 70, same as F070ZWE0 with only F-region zonal winds but replaced by E-region conductivity (COEr) at Z_p < −2 from F200STD	Isolate the effect of the solar cycle change in E-region conductivity on the F-region zonal wind dynamo
9. F070ZWFr	$F_{10.7}$ = 70, same as F070ZWE0 with only F-region zonal winds but replaced by F-region zonal winds (ZWFr) at Z_p > −2 from F200STD	Isolate the effect of the solar cycle change in E-region conductivity on the F-region zonal wind dynamo

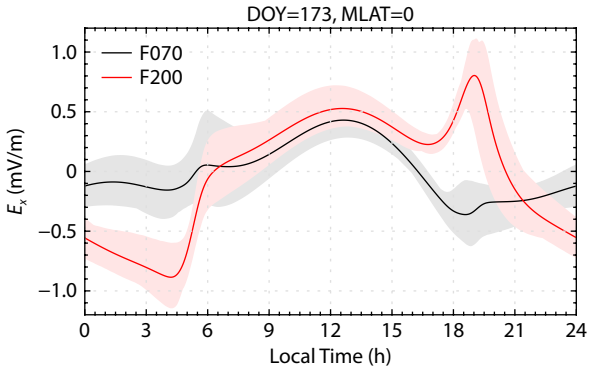

Figure 1. Diurnal variations in equatorial zonal electric fields (E_x) at solar minimum and maximum. All results are at the June solstice and magnetic equator from the runs with tidal effects at $F_{10.7}$ = 70 and 200. The gray and pink patches represent the data at all longitudes, and the black and red lines denote the longitude averages. DOY, day of year; MLAT, magnetic latitude.

between solar maximum and minimum at the June solstice is the greatest (−0.29 mV/m) near 90°W and the smallest (−0.02 mV/m) near 20°W. This longitudinal feature has been investigated and compared in detail with the observations by Chen JJ et al. (2021b).

Figure 2b shows the seasonal variation in the sunrise equatorial zonal electric field at 90°W, indicating that the sunrise enhancement occurs near the solstice and reaches a maximum in June for all solar activity levels. The direction of the sunrise equatorial zonal electric field changes to westward at the equinoxes. An increase in solar activity tends to make the sunrise equatorial zonal electric field more westward in all seasons. The ROCSAT-1 satellite data show that an increase in solar activity from $F_{10.7}$ = 130 to 200 induces a westward change of no larger than 1 mV/m in the long-term average sunrise zonal electric fields at most longitudes and in most seasons (see Fig. 7 in Fejer et al., 2008), which is generally consistent with the simulated solar cycle dependence in Figure 2. However, the long-term averages of the ROCSAT-1 observations do not show a sunrise enhancement. The sunrise enhancement did have an occurrence rate of 20%–30% in a statistical analysis using the same data set (Zhang RL et al., 2015) and is reproduced at the solstice by the TIEGCM (Chen JJ et al., 2020). This finding may indicate that the long-term average method may smooth out important features, such as the sunrise enhancement. This result may also be related to large measurement errors in the late night or early morning because of the low plasma density and increased light ion population (Fejer et al., 2008). The TIEGCM-simulated sunrise electric fields are not completely consistent with the long-term average observation, but the model does show the decreasing sunrise eastward electric fields with increasing solar activity.

Atmospheric tides, especially nonmigrating semidiurnal tides, can modulate the sunrise eastward enhancement of equatorial zonal electric fields (Liu HL and Richmond, 2013; Zhou X et al., 2020). To

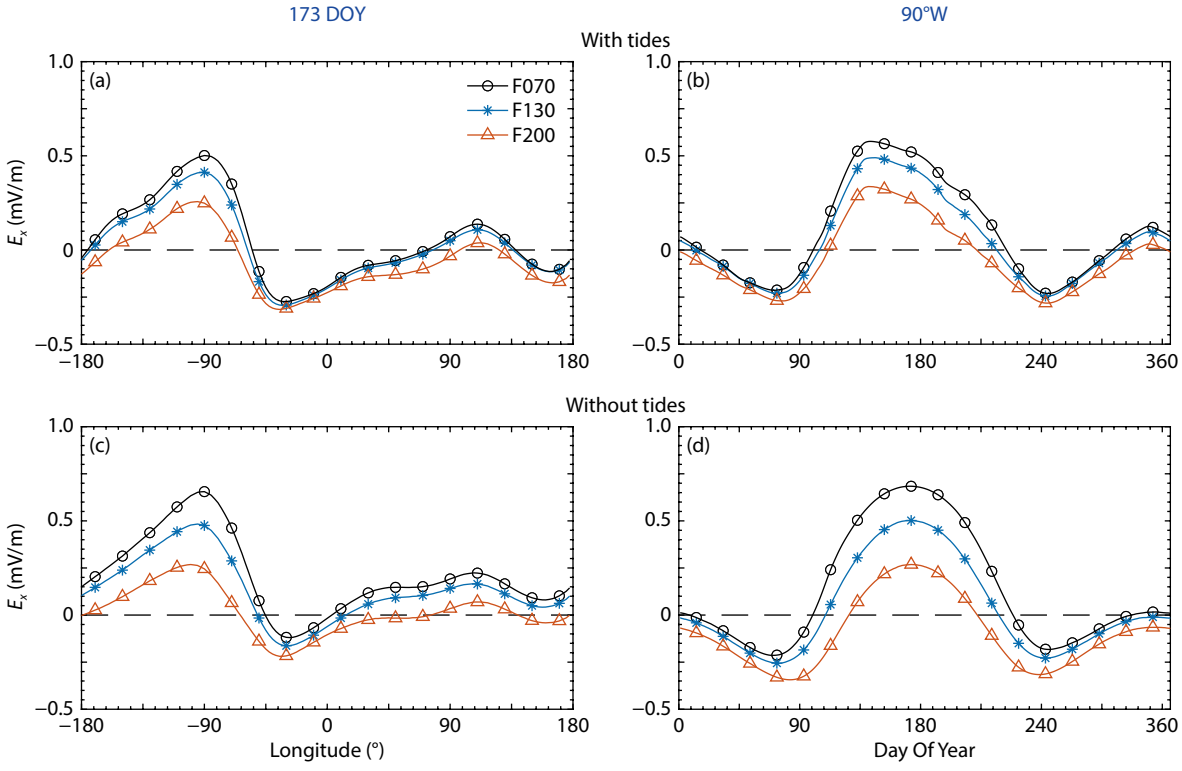

Figure 2. The ionospheric sunrise equatorial zonal electric field (E_x, positive eastward) at different solar activity levels. (left) Longitudinal variations at the June solstice (day of year (DOY) 173) and (right) seasonal variations at 90°W of the zonal electric fields from the simulations (top) with the tidal effects and (bottom) without the tidal effects. All results are at the dip equator, 6:00 LT, and pressure level 2 (~260–340 km, depending on solar activity near the F_2 layer). Lines with different colors and symbols represent different solar activity conditions ($F_{10.7}$ = 70, 130, and 200).

examine whether the solar cycle dependence of sunrise electric fields varies with atmospheric tidal conditions, we ran three simulations that were similar to the three runs in Figure 2a but that did not have empirical tidal forcing at the lower boundary. In these new cases, the solar EUV radiation (represented by the $F_{10.7}$ index) was the only external input that varied. The longitudinal and seasonal variations in equatorial zonal electric fields at 6:00 MLT under different solar activity conditions are shown in Figures 2c, d. The resulting longitudinal and seasonal variations in the simulated results without tidal effects are similar to those with tidal effects (cf. Figures 2a, b), although their values and peak locations do differ. At the June solstice, the sunrise equatorial electric fields reach an eastward maximum at 90°W for all cases. The electric field near 90°W has the largest eastward peak at the June solstice, with a second smaller peak occurring at the December solstice. As in the standard cases, the increase in solar EUV radiation reduces the sunrise zonal electric fields without tidal forcing for all longitudes and seasons (Figures 2c, d). Thus, lower atmospheric tides can modulate the magnitude of the sunrise enhancement, but they do not change the solar cycle dependence. Comparing the top row with the bottom row in Figure 2, the solar cycle variation in sunrise electric field enhancement is smaller when atmospheric tides are included. In summary, the simulation results in Figure 2 reveal that under geomagnetically quiet conditions (cross-polar cap potential of 0), the sunrise zonal electric field always decreases with increasing solar activity at all longitudes for different seasonal and tidal conditions.

3.2 The Influence of Different Wind Dynamo Sources

During geomagnetically quiet periods, the ionospheric electrodynamics is dominated by the neutral wind dynamo (Richmond, 1995a; Heelis, 2004). The sunrise enhancement of equatorial zonal electric fields is mainly caused by the zonal wind dynamo (Kelley et al., 2014; Chen JJ et al., 2020), but the relatively weak meridional wind dynamo cannot be ignored (Liu HL and Richmond, 2013; Chen JJ et al., 2020). To explore the solar cycle dependence of the sunrise electrodynamics driven by dynamo processes from zonal winds, two controlled simulations (F070MW0 and F200MW0) based on F070STD and F200STD were conducted, as shown in Table 1. The influence of the meridional wind dynamo at solar minimum (maximum) was obtained by subtracting F070MW0 from F070STD (F200MW0 from F200STD).

Figure 3a shows comparisons of the sunrise equatorial zonal electric field at solar minimum (dotted lines) and maximum (solid lines) driven by the full wind dynamo in the standard runs, by the zonal wind dynamo only, and by the meridional wind dynamo only. The zonal electric field differences between the solar maximum and minimum are shown in Figure 3b. At solar minimum, the equatorial zonal electric field in F070STD (dotted black line in Figure 3a) has a maximum of 0.68 mV/m at 6:00 MLT, whereas the zonal wind dynamo has a maximum of 0.56 mV/m (dotted red line). The meridional wind dynamo produces a zonal electric field of only 0.12 mV/m (dotted blue line). This result indicates that the sunrise enhancement at solar minimum (F070STD) comes mainly from the zonal wind dynamo. At solar maximum, the sunrise equatorial eastward electric field in F200STD is only 0.27 mV/m (solid black line in Figure 3a). The contribution of the zonal wind dynamo (0.20 mV/m) to the overall sunrise eastward electric field at solar maximum (F200STD) is again greater than the meridional wind dynamo effect (0.07 mV/m). Figure 3b shows that the difference in zonal electric fields between the solar maximum and minimum attributable to the zonal wind dynamo (red line) is −0.36 mV/m, which is much larger than the electric field difference of −0.05 mV/m caused by the meridional wind dynamo (blue line). Hence, the solar cycle variation in the sunrise enhancement of the ionospheric equatorial zonal electric fields mainly depends on the solar cycle variation in the zonal wind dynamo.

The midlatitude E-region zonal wind dynamo has been found to be the major source of the sunrise (4:00–8:00 LT) enhancement of equatorial zonal electric fields at solar minimum (Liu HL and Richmond, 2013; Chen JJ et al., 2020; Zhou X et al., 2020). However, the local equatorial F-region dynamo may also affect sunrise electric fields (Kelley et al., 2014) because the presunrise (4:00–6:00 LT) Pedersen conductivity is usually larger in the F-region than in the E-region (Heelis, 2004). The solar cycle dependence of the E-region and F-region dynamo effects around sunrise were further quantified with two simulations (F070ZWE0 and F200ZWE0). In both runs, the wind-driven source currents for the stand-alone dynamo module were driven by zonal winds only above pressure level −2 (greater than ~150 km) to produce only F-region zonal wind effects. The contribution of the E-region zonal wind dynamo to the electrodynamics at solar minimum (maximum) was separated by subtracting F070ZWE0 from F070MW0 (F200ZWE from F200MW0).

The equatorial zonal electric fields driven by the full zonal wind dynamo, the F-region zonal wind dynamo only, or the E-region zonal wind dynamo only under solar minimum (dotted lines) and maximum (solid lines) conditions are shown in Figure 3c. Figure 3d displays zonal electric field differences between solar maximum and minimum. Figure 3c shows that at solar minimum, the sunrise zonal electric field generated by the zonal wind dynamo (dotted red) reaches 0.56 mV/m, which is primarily produced by the E-region dynamo effect of 0.42 mV/m (dotted green), whereas the F-region dynamo produces only a weak electric field of 0.14 mV/m (dotted yellow). At solar maximum, the zonal electric field near sunrise has a value of 0.20 mV/m caused by the zonal wind dynamo (solid red), which includes two sources, an eastward electric field (E_x) of 0.33 mV/m related to the E-region dynamo (solid green) and a westward one of −0.13 mV/m generated by the F-region effect (solid yellow). The E-region zonal wind dynamo is again the major process in the sunrise enhancement of equatorial eastward electric fields, which is consistent with the generation mechanism of equatorial sunrise enhancement proposed by Chen JJ et al. (2020). However, as shown in Figure 3d, it is interesting to note that the solar cycle difference in the sunrise zonal electric fields related to the E-region zonal wind dynamo is only −0.09 mV /m (green line), which is much weaker than the electric field difference of −0.27 mV/m associated with the F-region zonal wind dynamo (yellow line). This result suggests that the sunrise zonal wind dynamo in the F-region has a greater response to the solar cycle change in EUV radiation than does the E-region dynamo. Specifically, the E-region zonal wind dynamo tends to produce a westward equatorial electric field at 6:00 MLT at solar maximum,

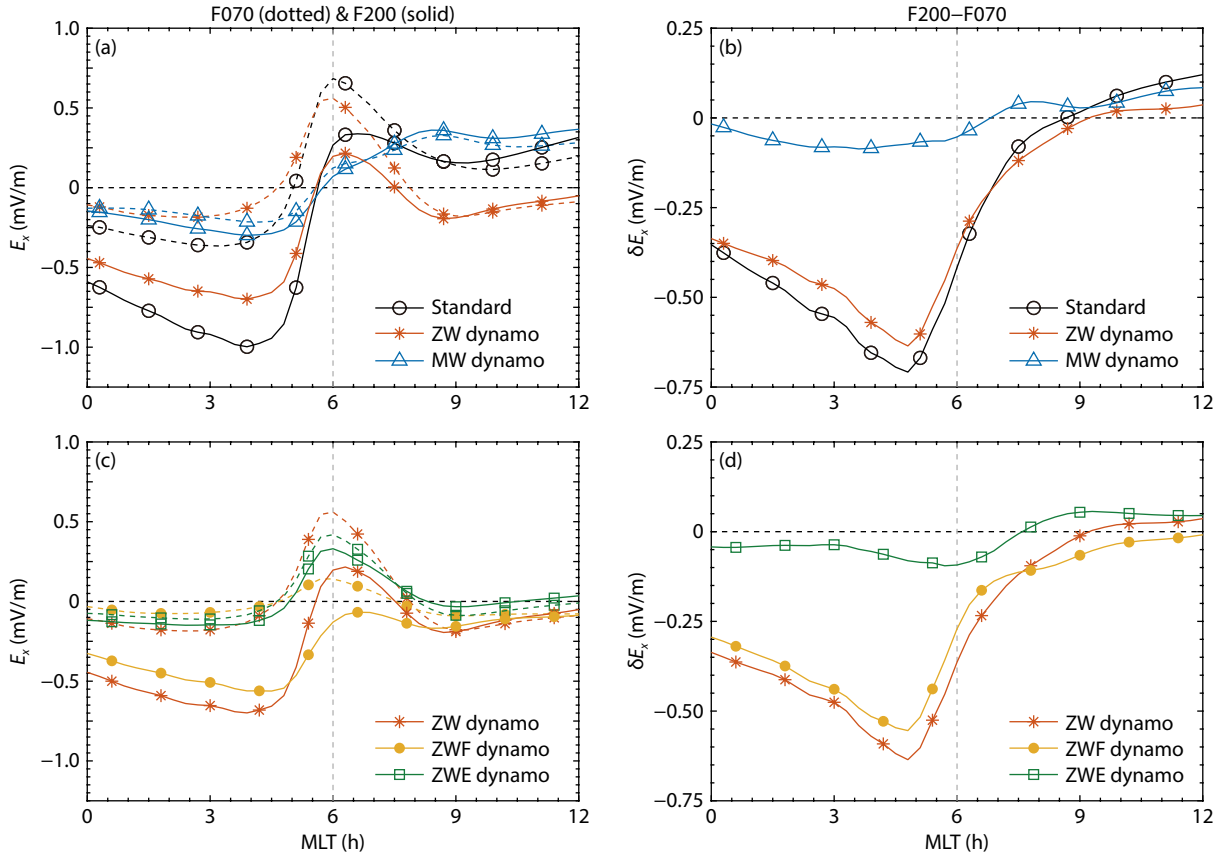

Figure 3. Solar cycle dependence of the equatorial zonal electric field (E_x) driven by different wind dynamo sources. (left) The magnetic local time (MLT) variation of E_x by the full wind dynamo in the standard runs (F070STD and F200STD), zonal wind dynamo only (F070MW0 and F200MW0), meridional wind dynamo only (F070STD–F070MW0 and F200STD–F200MW0), F-region zonal wind dynamo only (F070ZWE0 and F200ZWE0), and E-region zonal wind dynamo only (F070MW0–F070ZWE0 and F200MW0–F200ZWE0) at solar minimum (F070, dotted line) and maximum (F200, solid line). (right) The corresponding E_x difference (δE_x) caused by the different processes between solar maximum and minimum (F200–F070). All results are at the June solstice, 0° magnetic latitude, pressure level 2, and 12:00 UT, when 6:00 MLT corresponds to 6:00 LT at 90°W. The vertical dashed gray line denotes the sunrise time of 6:00 MLT. ZW, zonal wind; MW, meridional wind; ZWF, F-region zonal wind dynamo; ZWE, E-region zonal wind dynamo.

which is opposite the effect at solar minimum, as discussed in Section 4. In summary, the sunrise enhancement is mainly driven by the E-region zonal wind dynamo, but its solar cycle dependence is dominated by the solar cycle response of the F-region dynamo.

3.3 Contributions of Solar Cycle Variations in Neutral Winds and Conductivity

Changes in the wind dynamo are directly associated with variations in neutral winds and conductivity (e.g., Richmond, 1995a). Figure 4 shows solar cycle variations in Pedersen conductivity (σ_P), zonal winds (U_x), and Pedersen conductivity-weighted zonal winds ($\frac{\sigma_P U_x}{\Sigma_P}$, where Σ_P is the height-integrated Pedersen conductance) near sunrise at midlatitudes (top row) and the dip equator (bottom row). The expression $\frac{\sigma_P U_x}{\Sigma_P}$ can roughly represent the relative contribution of zonal winds at a given altitude to the overall dynamo process, as described by Chen JJ et al. (2021a). When solar activity increases from 70 to 200, the Pedersen conductivity and neutral winds near the dawn terminator show a significant response above ~150 km altitude, as well as in pressure coordinates (not shown), but the relative change below ~150 km is much smaller. In general, the magnitude of $\frac{\sigma_P U_x}{\Sigma_P}$ shows a significant increase above ~170 km and a decrease or a very small change below ~170 km (Figures 4c, f). Figure 4c shows that at middle latitudes, the increase in $\frac{\sigma_P U_x}{\Sigma_P}$ above ~170 km and the decrease at ~120–170 km are comparable. However, for low latitudes, solar cycle changes in $\frac{\sigma_P U_x}{\Sigma_P}$ in the E-region are much weaker than in the F-region (Figure 4f). Solar cycle changes of $\frac{\sigma_P U_x}{\Sigma_P}$ are consistent with the solar cycle variations in the electric field driven by F-region and E-region dynamos in Figures 3c, d.

To further isolate the effects of the zonal wind or conductivity variation at different altitudes on the F-region zonal wind dynamo, three controlled simulations (F070COFr, F070COEr, and F070ZWFr) were carried out. As listed in Table 1, they are based on the solar minimum simulation with only the F-region zonal wind dynamo effect (F070ZWE0) but replaced with conductivity or zonal wind inputs from the solar maximum standard run (F200STD). For example, inputs for the stand-alone dynamo module in F070COFr were mostly the same as those in F070ZWE0, but the F-region

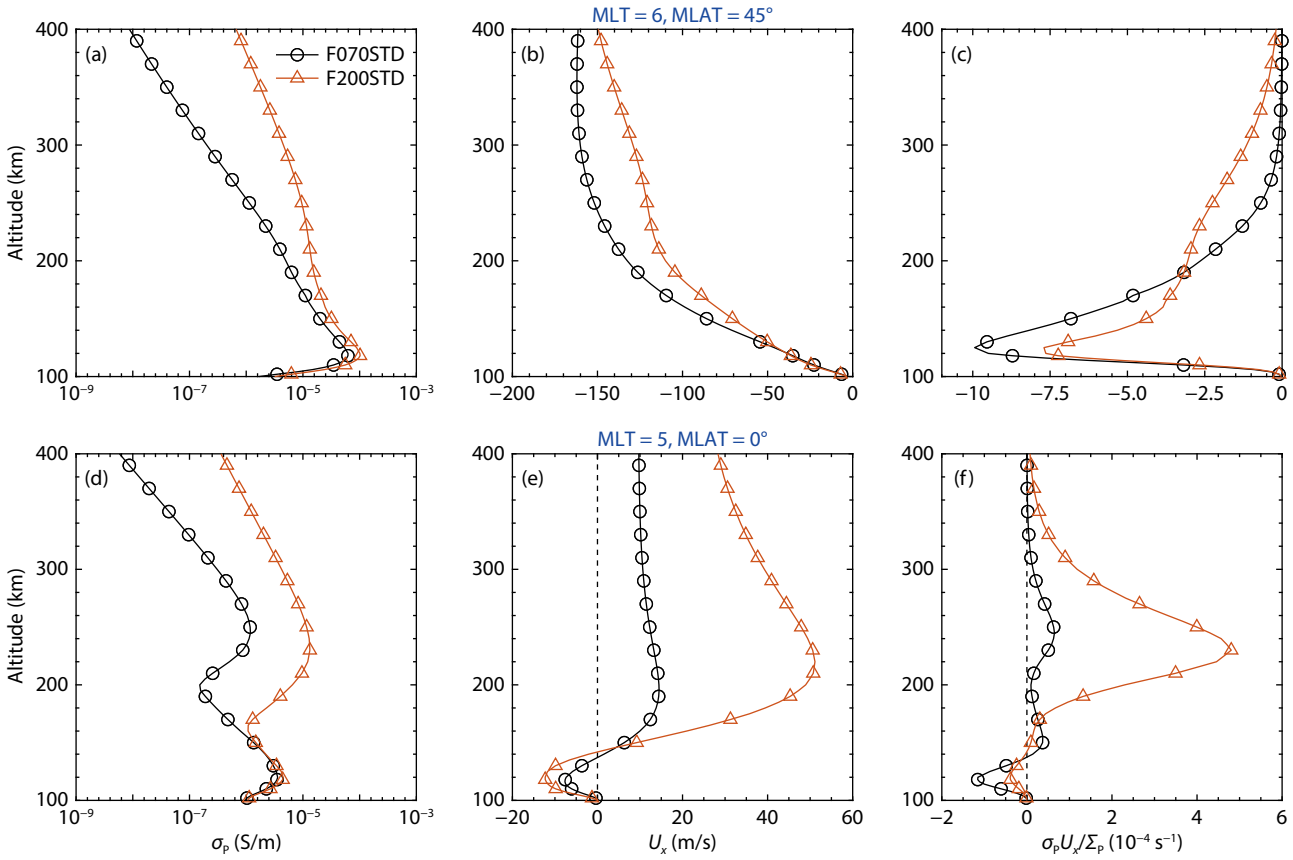

Figure 4. Solar cycle dependence of the conductivity and neutral winds. Altitudinal variations of Pedersen conductivity (σ_P, left column), zonal winds (U_x, positive eastward, middle column), and Pedersen conductivity-weighted zonal winds ($\frac{\sigma_P U_x}{\Sigma_P}$, positive eastward, right column) in F070STD (same as in F070MW0) and F200STD (same as in F200MW0) at 12:00 UT. (Top row) At 6:00 magnetic local time (MLT) and 45° magnetic latitude (MLAT). (Bottom row) At 5:00 MLT and 0° MLAT.

conductivity input above pressure level −2 (greater than ~150 km) was replaced by the ones from F200STD. In this way, the electric field difference between F070COFr and F070ZWE0 (F070COFr – F070ZWE0) is caused only by the solar cycle variation in the F-region conductivity. Similarly, the effects of solar cycle changes in the E-region conductivity (F070COEr–F070ZWE0) and F-region zonal winds (F070ZWFr–F070ZWE0) on the solar cycle variation in the F-region zonal wind dynamo are isolated in F070COEr and F070ZWFr, respectively. Obviously, the E-region wind variation has no direct contribution to the F-region dynamo.

Figure 5 shows the contribution of solar cycle changes in F-region conductivity, E-region conductivity, and F-region zonal winds to the equatorial zonal electric field difference (δE_x) driven by the F-region zonal wind dynamo between the solar maximum and minimum (F200ZWE0–F070ZWE0). The δE_x attributable to both wind and conductivity changes (yellow line) reaches −0.27 mV/m at 6:00 MLT, but with a minimum of −0.55 mV/m near 5:00 MLT. The F-region conductivity changes (black line) generate an δE_x of −0.05 mV/m at 6:00 MLT and a roughly constant value of approximately −0.3 mV/m before 5:00 MLT, whereas the δE_x caused by solar cycle changes in zonal winds (F070ZWFr–F070ZWE0) is −0.14 mV/m at 6:00 MLT and has a westward enhancement of −0.22 mV/m at 5:00 MLT. The contribution from the E-region conductivity changes (F070COEr–F070ZWE0) is negligible with

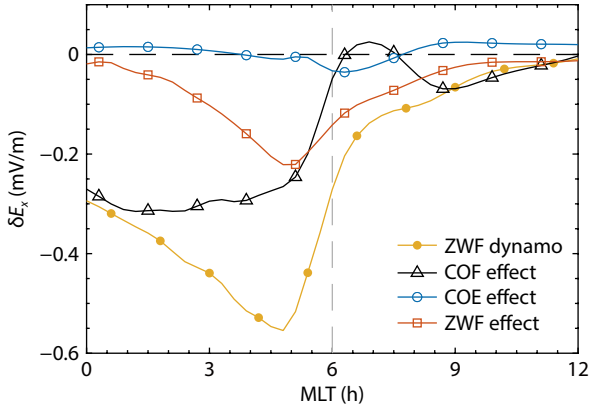

Figure 5. Effects of the solar cycle variations in conductivity and neutral winds at different altitudes on equatorial zonal electric fields. The yellow, black, blue, and red lines show the difference in zonal electric fields (δE_x) between four controlled simulations (F200ZWE0, F070COFr, F070COEr, and F070ZEFr) and F070ZWE0, which corresponds to the F-region zonal wind dynamo difference between solar maximum and minimum, and the contributions of the changes in F-region conductivity (COF), E-region conductivity (COE), and F-region zonal wind variations (ZWF), respectively. All results are at the dip equator, pressure level 2, 12:00 UT, and the June solstice. MLT, magnetic local time.

respect to the other two effects. Solar cycle changes in conductivity and zonal winds in the F-region are larger than those in the E-region near sunrise (Figure 5); thus, they are important for the solar cycle dependence of the F-region zonal wind dynamo near sunrise. Overall, increasing solar EUV radiation decreases equatorial zonal electric fields near and before sunrise, which is mainly induced by both F-region conductivity and zonal wind changes.

4. Discussion

Figure 1 shows that both the sunrise and sunset equatorial zonal electric field enhancements usually have a prominent eastward enhancement on the order of 1 mV/m. At sunset, it is called the prereversal enhancement (PRE; Heelis et al., 1974; Fejer et al., 1979, 1991, 2008; Eccles, 1998; Fesen et al., 2000). The sunset PRE is much stronger at solar maximum than at solar minimum, which is opposite the solar cycle dependence of sunrise equatorial electric fields seen in most satellite observations (Fejer et al., 2008; Kil et al., 2009) and the TIEGCM simulations. An important issue to address is why equatorial zonal electric fields near the dawn and dusk terminators show an opposite solar cycle dependence.

The opposite solar cycle responses of eastward electric field enhancements near dawn and dusk terminators are associated with their different generation mechanisms. Near sunset, the equatorial eastward PRE is mainly driven by the F-region zonal wind dynamo locally near the equator (Farley et al., 1986; Eccles, 1998; Heelis et al., 2012; Eccles et al., 2015). Nevertheless, the sunrise enhancement at the dip equator is primarily driven by the midlatitude E-region zonal wind dynamo, as shown in Figures 3a, b and previous studies (Liu HL and Richmond, 2013; Chen JJ et al., 2020). The equatorial F-region zonal wind dynamo tends to induce sunrise westward electric fields that are more pronounced at solar maximum (Figures 3c, d). Near both sunrise and sunset, increasing EUV with solar activity can significantly increase F-region conductance, which increases the relative importance of the F-region dynamo and decreases the E-region dynamo effect (Figure 4). As a result, the zonal electric fields at sunrise show variations opposite those at sunset in terms of solar cycle dependence.

To further explain the different generation mechanisms for the sunrise and sunset eastward enhancement, Figure 6 shows the global zonal electric fields (E_x), Pedersen conductivity-weighted $(\boldsymbol{U}\times\boldsymbol{B})_{\perp y}$ ($(\boldsymbol{U}\times\boldsymbol{B})^{\mathrm{P}}_{\perp y}$, cf. Equation (4)), and Pedersen conductance (Σ_{P}) from the runs with only the zonal wind dynamo. The $(\boldsymbol{U}\times\boldsymbol{B})^{\mathrm{P}}_{\perp y}$ can roughly represent the overall zonal wind dynamo effect at different altitudes, as described by Chen JJ et al. (2021a). The sunset PRE is mainly explained by the curl-free mechanism (Heelis et al., 2012; Eccles et al., 2015; Chen JJ and Lei JH, 2019) and is secondarily related to the Hall current divergence mechanism (e.g., Farley et al., 1986; Eccles et al., 2015). In the curl-free theory, the eastward MLT gradient of low-latitude F-region zonal winds and the large gradient of conductance near sunset generate a local equatorial eastward PRE (Heelis et al., 2012; Eccles et al., 2015). This process corresponds to the low-latitude E_x, $(\boldsymbol{U}\times\boldsymbol{B})^{\mathrm{P}}_{\perp y}$, and Σ_{P} around 19:00 MLT in Figure 6. The sunrise F-region dynamo can also be explained by a similar mechanism responsible for the sunset PRE. At low latitudes, increasing solar EUV radiation induces westward variations in the MLT gradient of F-region zonal winds near sunrise, which corresponds to the MLT gradient of equatorial $\delta(\boldsymbol{U}\times\boldsymbol{B})^{\mathrm{P}}_{\perp y}$ at 3:00–7:00 MLT in Figure 6f. According to the curl-free theory, this sunrise F-region wind gradient produces a local westward enhancement of equatorial zonal electric fields (Figure 6c). Similar prominent westward enhancements of zonal electric fields on the order of 1.0 mV/m during presunrise periods have been observed (Prabhakaran Nayar et al., 2009; Mathew et al., 2010). The great speed and MLT gradient of E-region westward winds and the associated equatorward $(\boldsymbol{U}\times\boldsymbol{B})^{\mathrm{P}}_{\perp y}$ at middle latitudes (Figures 6d, e), in conjunction with the declination of the dawn termination that constrains the conductance (Figures 6g, h), locally produce strong midlatitude eastward electric fields that can penetrate to lower latitudes and even the magnetic equator (Figures 6a, b). This process is described in detail by Chen JJ et al. (2020).

The direction and solar cycle dependence of the sunrise equatorial zonal electric field is complicated by the competition between the E-region and F-region dynamos. Twelve o'clock universal time (UT) at the June solstice, the time when the simulated equatorial sunrise enhancement is the strongest, is used as an example in Figure 6. At 6:00 MLT and 45° magnetic latitude (MLAT), where the sunrise eastward enhancement reaches a maximum (Figures 6a, b), the E-region (<150 km) Pedersen conductance is approximately 3 times as large as the F-region (>150 km) conductance in Figure 4a. Thus, the midlatitude zonal wind dynamo near 6:00 MLT is determined by the E-region zonal winds. As the solar EUV radiation increases, the sunrise eastward electric field driven by the midlatitude E-region dynamo is suppressed by the increase in F-region conductivity at midlatitudes (black line in Figure 5), which was also suggested by Liu HL and Richmond (2013). But these electric fields are also enhanced by the increase in E-region conductivity and are slightly modulated by the changes in zonal winds (blue and red lines in Figure 5). In general, solar activity variations in the F-region and E-region dynamo effects are generally offset by each other at midlatitude (Figures 4c, 6c, f), which explains why the midlatitude $(\boldsymbol{U}\times\boldsymbol{B})^{\mathrm{P}}_{\perp y}$ and the resultant zonal electric fields near 6:00 MLT are similar between the solar minimum and maximum (see the top and middle rows in Figure 6). At 5:00 MLT and 0° MLAT, where the reduction of zonal electric fields with increasing solar activity is the most obvious (see Figure 6c), zonal winds are westward below ~140 km and turn eastward above ~140 km (middle column in Figure 4). At solar minimum, the Pedersen conductance below 140 km (0.10 S) is only slightly smaller than that above 140 km (0.14 S) and the zonal wind speeds in the E-region and F-region are comparable. Thus, local zonal wind dynamo effects in the E-region and F-region are partially balanced out, which causes weak magnitudes of $(\boldsymbol{U}\times\boldsymbol{B})^{\mathrm{P}}_{\perp y}$ (Figure 6d) and westward E_x (Figure 6a) in presunrise equatorial regions. Note that the eastward equatorial electric field at 6:00 MLT is mainly from the midlatitude dynamo rather than being a local effect (Chen JJ et al., 2020). When solar activity increases from $F_{10.7}$ = 70 to 200, both Pedersen conductivity and zonal winds do not change in the E-region (<150 km) but have a large enhancement in the F-region (>150 km), as shown in Figure 4. This enhancement strengthens the effect of the F-region zonal wind dynamo on local zonal electric

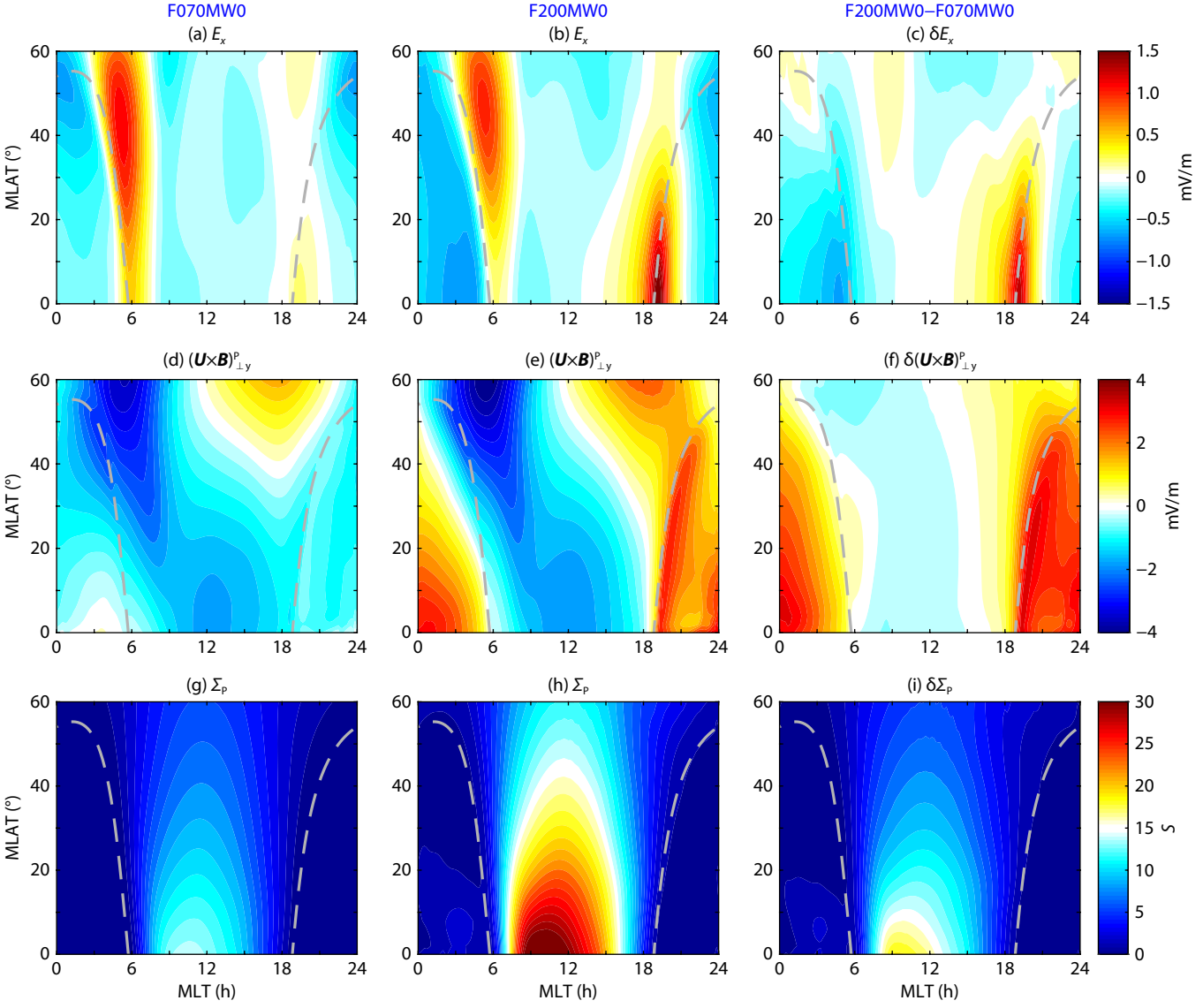

Figure 6. Solar cycle dependence of global zonal electric fields and the driving processes. From top to bottom: zonal electric fields (E_x, positive eastward, top row) at pressure level 2, hemispheric height-integrated Pedersen conductivity-weighted $(\boldsymbol{U}\times\boldsymbol{B})_{\perp y}$ ($(\boldsymbol{U}\times\boldsymbol{B})^{P}_{\perp y}$, middle row), and hemispheric Pedersen conductance (Σ_P, bottom row) from the runs with the zonal wind dynamo only at solar minimum (F070MW0, left column) and maximum (F200MW0, middle column) in magnetic latitude (MLAT)–magnetic local time (MLT) coordinates at 12:00 UT at the June solstice. The right column denotes the difference in E_x, $(\boldsymbol{U}\times\boldsymbol{B})^{P}_{\perp y}$, and Σ_P between F200MW0 and F070MW0. The dashed gray line denotes the E-region terminator (solar zenith angle = 98°).

fields, corresponding to large changes in the F-region $\frac{\sigma_P U_x}{\Sigma_P}$ (Figure 4f), $(\boldsymbol{U}\times\boldsymbol{B})^{P}_{\perp y}$ (Figure 6f), and zonal electric fields (Figure 6c) at low latitudes near and before sunrise. Combining Figures 3 and 7a in Chen JJ et al. (2021b), even at solar minimum in June, the low-latitude dynamo effect can exceed the midlatitude effect and produce westward equatorial electric fields at 6:00 MLT near 30°W. Hence, the F-region dynamo effect at low latitudes is complex and varies with longitude.

Three puzzles remain in the comparison between the simulations and the observations. The first is why the solar cycle variation in the long-term and longitude average of ROCSAT-1 data (Fejer et al., 2008; Kil et al., 2009) is not as obvious as in the model (Figure 2). The top row of Figure 2 shows that the difference in the simulated zonal electric field at sunrise between $F_{10.7}$ = 200 and $F_{10.7}$ = 130 is not larger than 0.15 mV/m, which is much smaller than the maximum longitudinal and seasonal differences of ~0.8 mV/m. This result might partly explain why the observed solar cycle variation in the average data is weak. In addition, this fact is probably a consequence of potential measurement error in the late night or early morning caused by the low plasma density and increased light ion population, as pointed out by Fejer et al. (2008), and altitudinal variations in the satellite position in different years. Second, from an observational point of view, the sunrise enhancement is not always present in the electric field (Zhang RL et al., 2015). The question is then how to account for this factor in the simulation to characterize the solar cycle dependency of the occurrence of the sunrise eastward enhancement. The increase in

solar flux only slightly decreases the electric field at 6:00 LT by < 0.15 mV/m, but it significantly varies the electric field structure near the dawn terminator by affecting the F-region dynamo, which suppresses the occurrence of the sunrise eastward enhancement (Figures 1, 3). The third question is why our simulations do not show eastward enhancement near equinoxes, whereas the statistical occurrence rate of the enhancement in observations is at least 20% (Zhang RL et al., 2015). This simulation –observation difference should be related to the effects of day-to-day variability in lower atmospheric tides (Zhou X et al., 2020) and geomagnetic disturbances, which could induce additional eastward electric field disturbances (Liu HL and Richmond, 2013; Chen JJ et al., 2020). The tidal input in the empirical Global Scale Wave Model for the TIEGCM is the monthly mean without daily variability, which might cause the TIEGCM to lack some electrodynamic responses of the thermosphere–ionosphere system to real lower atmospheric tides. Furthermore, the effects of penetration electric fields and a disturbance wind dynamo, which also affect the sunrise enhancement (Chen JJ et al., 2020), were turned off in our simulations, but these influences are included in the observation results (Zhang RL et al., 2015) under geomagnetic conditions with $Kp < 4$. The effects of the day-to-day variability in lower atmospheric tides and geomagnetic disturbances still need further investigation.

5. Summary

In this study, a series of first-principle TIEGCM numerical experiments were carried out to investigate the physical mechanisms by which increasing solar activity causes a reduction in equatorial eastward zonal electric fields at sunrise during geomagnetically quiet periods. The main conclusions are as follows:

(1) As solar activity increases, the equatorial eastward electric field near sunrise decreases or turns westward independent of longitude, season, and lower atmospheric tides.

(2) The eastward reduction or westward enhancement of sunrise equatorial electric fields with increasing solar activity is mainly caused by the variation in the zonal wind dynamo with solar activity. Moreover, this variation in the zonal wind dynamo near sunrise is dominated by the corresponding variation in the F-region dynamo rather than the E-region dynamo, although the sunrise eastward enhancement of electric fields is mainly driven by the E-region zonal wind dynamo.

(3) The sunrise E-region zonal wind dynamo, which is mainly associated with the midlatitude dynamo, generates an eastward enhancement of the equatorial zonal electric field. The sunrise E-region electrodynamics decreases slightly with increasing solar activity because of the increase in midlatitude F-region conductance.

(4) The equatorial F-region zonal wind dynamo at sunrise produces a local westward enhancement of electric fields according to the curl-free electric field mechanism, which is associated with the westward gradient of F-region zonal winds near the dawn terminator. This westward electric field in the equatorial region, dominated by the variation in F-region (>150 km) conductivity and zonal winds at low latitudes near sunrise, is not obvious during solar minimum but becomes significant as solar activity increases.

In summary, the reduction in equatorial eastward electric fields near sunrise with increasing solar activity is mainly caused by the significant variation in the low-latitude F-region zonal wind dynamo resulting from changes in the F-region conductivity and zonal winds as well from solar activity.

Acknowledgments

This work was supported by the National Natural Science Foundation of China (Grant Nos. 42188101 and 41974181), the B-type Strategic Priority Program of the Chinese Academy of Sciences (CAS, Grant No. XDB41000000), the Project of Stable Support for Youth Team in Basic Research Field, CAS (Grant No. YSBR-018), the preresearch project on Civil Aerospace Technologies (Grant No. D020105) funded by China's National Space Administration, and the International Partnership Program of CAS (Grant No. 183311KYSB20200003). The National Center for Atmospheric Research is sponsored by the National Science Foundation. The TIEGCM simulation data and analysis routines are available online (https://doi.org/10.17605/OSF.IO/6YZQW). We thank Phil Richards for his comments on the manuscript.

References

Aggson, T. L., Herrero, F. A., Johnson, J. A., Pfaff, R. F., Laakso, H., Maynard, N. C., and Moses, J. J. (1995). Satellite observations of zonal electric fields near sunrise in the equatorial ionosphere. *J. Atmos. Terr. Phys.*, *57*(1), 19–24. https://doi.org/10.1016/0021-9169(93)E0013-Y

Baker, W. G., and Martyn, D. F. (1953). Electric currents in the ionosphere—the conductivity. *Philos. Trans. Roy. Soc. London Ser. A Math. Phys. Sci.*, *246*(913), 281–294. https://doi.org/10.1098/rsta.1953.0016

Chen, J. J., and Lei, J. H. (2019). A simulation study on the latitudinal variations of ionospheric zonal electric fields under geomagnetically quiet conditions. *J. Geophys. Res.: Space Phys.*, *124*(2), 1444–1453. https://doi.org/10.1029/2018ja026174

Chen, J. J., Wang, W. B., Lei, J. H., and Dang, T. (2020). The physical mechanisms for the sunrise enhancement of equatorial ionospheric upward vertical drifts. *J. Geophys. Res.: Space Phys.*, *125*(8), e2020JA028161. https://doi.org/10.1029/2020ja028161

Chen, J. J., Lei, J. H., Wang, W. B., Liu, J., Maute, A., Qian, L. Y., Zhang, R. L., and Dang, T. (2021a). Ionospheric electrodynamic response to solar flares in September 2017. *J. Geophys. Res.: Space Phys.*, *126*(11), e2021JA029745. https://doi.org/10.1029/2021JA029745

Chen, J. J., Wang, W. B., and Lei, J. H. (2021b). Longitudinal variations of equatorial ionospheric electric fields near sunrise. *J. Geophys. Res.: Space Phys.*, *126*(5), e2020JA028977. https://doi.org/10.1029/2020JA028977

Dang, T., Luan, X. L., Lei, J. H., Dou, X. K., and Wan, W. X. (2016). A numerical study of the interhemispheric asymmetry of the equatorial ionization anomaly in solstice at solar minimum. *J. Geophys. Res.: Space Phys.*, *121*(9), 9099–9110. https://doi.org/10.1002/2016ja023012

De Adler, N. O., Elías, A. G., and Manzano, J. R. (1997). Solar cycle length variation: its relation with ionospheric parameters. *J. Atmos. Sol. Terr. Phys.*, *59*(2), 159–162. https://doi.org/10.1016/S1364-6826(96)00056-9

Drob, D. P., Emmert, J. T., Meriwether, J. W., Makela, J. J., Doornbos, E., Conde, M., Hernandez, G., Noto, J., Zawdie, K. A., … Klenzing, J. H. (2015). An update to the Horizontal Wind Model (HWM): the quiet time thermosphere. *Earth and Space Science*, *2*(7), 301–319. https://doi.org/10.1002/2014ea000089

Eccles, J. V. (1998). Modeling investigation of the evening prereversal enhancement of the zonal electric field in the equatorial ionosphere. *J. Geophys. Res.: Space Phys.*, *103*(A11), 26709–26719. https://doi.org/10.1029/98ja02656

Eccles, J. V., St. Maurice, J. P., and Schunk, R. W. (2015). Mechanisms underlying the prereversal enhancement of the vertical plasma drift in the low-latitude ionosphere. *J. Geophys. Res.*: *Space Phys.*, *120*(6), 4950–4970. https://doi.org/10.1002/2014ja020664

Fang, T. W., Fuller-Rowell, T., Wang, H. J., Akmaev, R., and Wu, F. (2014). Ionospheric response to sudden stratospheric warming events at low and high solar activity. *J. Geophys. Res.*: *Space Phys.*, *119*(9), 7858–7869. https://doi.org/10.1002/2014JA020142

Farley, D. T., Bonelli, E., Fejer, B. G., and Larsen, M. F. (1986). The prereversal enhancement of the zonal electric field in the equatorial ionosphere. *J. Geophys. Res.*: *Space Phys.*, *91*(A12), 13723–13728. https://doi.org/10.1029/JA091iA12p13723

Fejer, B. G., Farley, D. T., Woodman, R. F., and Calderon, C. (1979). Dependence of equatorial *F* region vertical drifts on season and solar cycle. *J. Geophys. Res.*: *Space Phys.*, *84*(A10), 5792–5796. https://doi.org/10.1029/JA084iA10p05792

Fejer, B. G., De Paula, E. R., González, S. A., and Woodman, R. F. (1991). Average vertical and zonal F region plasma drifts over Jicamarca. *J. Geophys. Res.*: *Space Phys.*, *96*(A8), 13901–13906. https://doi.org/10.1029/91ja01171

Fejer, B. G., Jensen, J. W., and Su, S. Y. (2008). Quiet time equatorial *F* region vertical plasma drift model derived from ROCSAT-1 observations. *J. Geophys. Res.*: *Space Phys.*, *113*(A5), A05304. https://doi.org/10.1029/2007ja012801

Fesen, C. G., Crowley, G., Roble, R. G., Richmond, A. D., and Fejer, B. G. (2000). Simulation of the pre-reversal enhancement in the low latitude vertical ion drifts. *Geophys. Res. Lett.*, *27*(13), 1851–1854. https://doi.org/10.1029/2000gl000061

Hagan, M. E., and Oliver, W. L. (1985). Solar cycle variability of exospheric temperature at Millstone Hill between 1970 and 1980. *J. Geophys. Res.*: *Space Phys*, *90*(A12), 12265–12270. https://doi.org/10.1029/JA090iA12p12265

Hagan, M. E., and Forbes, J. M. (2002). Migrating and nonmigrating diurnal tides in the middle and upper atmosphere excited by tropospheric latent heat release. *J. Geophys. Res.*: *Atmos.*, *107*(D24), 4754. https://doi.org/10.1029/2001jd001236

Hagan, M. E., and Forbes, J. M. (2003). Migrating and nonmigrating semidiurnal tides in the upper atmosphere excited by tropospheric latent heat release. *J. Geophys. Res.*: *Space Phys.*, *108*(A2), 1062. https://doi.org/10.1029/2002ja009466

Hedin, A. E., and Mayr, H. G. (1987). Solar EUV induced variations in the thermosphere. *J. Geophys. Res.*: *Atmos.*, *92*(D1), 869–875. https://doi.org/10.1029/JD092iD01p00869

Hedin, A. E., Buonsanto, M. J., Codrescu, M., Duboin, M. L., Fesen, C. G., Hagan, M. E., Miller, K. L., and Sipler, D. P. (1994). Solar activity variations in midlatitude thermospheric meridional winds. *J. Geophys. Res.*: *Space Phys.*, *99*(A9), 17601–17608. https://doi.org/10.1029/94JA01134

Heelis, R. A., Kendall, P. C., Moffett, R. J., Windle, D. W., and Rishbeth, H. (1974). Electrical coupling of the *E*- and *F*-regions and its effect on *F*-region drifts and winds. *Planet. Space Sci.*, *22*(5), 743–756. https://doi.org/10.1016/0032-0633(74)90144-5

Heelis, R. A. (2004). Electrodynamics in the low and middle latitude ionosphere: a tutorial. *J. Atmos. Sol. Terr. Phys.*, *66*(10), 825–838. https://doi.org/10.1016/j.jastp.2004.01.034

Heelis, R. A., Crowley, G., Rodrigues, F., Reynolds, A., Wilder, R., Azeem, I., and Maute, A. (2012). The role of zonal winds in the production of a pre-reversal enhancement in the vertical ion drift in the low latitude ionosphere. *J. Geophys. Res.*: *Space Phys.*, *117*(A8), A08308. https://doi.org/10.1029/2012ja017547

Jiang, G. Y., Xu, J. Y., Wang, W. B., Yuan, W., Zhang, S. R., Yu, T., Zhang, X. X., Huang, C., Kerr, R. B., … Li, Q. Z. (2018). A comparison of quiet time thermospheric winds between FPI observations and model calculations. *J. Geophys. Res.*: *Space Phys.*, *123*(9), 7789–7805. https://doi.org/10.1029/2018ja025424

Kelley, M. C. (2009). *The Earth's Ionosphere*: *Plasma Physics and Electrodynamics* (2nd ed). San Diego: Academic Press.

Kelley, M. C., Rodrigues, F. S., Pfaff, R. F., and Klenzing, J. (2014). Observations of the generation of eastward equatorial electric fields near dawn. *Ann. Geophys.*, *32*(9), 1169–1175. https://doi.org/10.5194/angeo-32-1169-2014

Kil, H., Oh, S. J., Paxton, L. J., and Fang, T. W. (2009). High-resolution vertical $\mathbf{E}\times\mathbf{B}$ drift model derived from ROCSAT-1 data. *J. Geophys. Res.*: *Space Phys.*, *114*(A10), A10314. https://doi.org/10.1029/2009JA014324

Lei, J. H., Roble, R. G., Kawamura, S., and Fukao, S. (2007). A simulation study of thermospheric neutral winds over the MU radar. *J. Geophys. Res.*: *Space Phys.*, *112*(A4), A04303. https://doi.org/10.1029/2006ja012038

Liu, H. L., and Richmond, A. D. (2013). Attribution of ionospheric vertical plasma drift perturbations to large-scale waves and the dependence on solar activity. *J. Geophys. Res.*: *Space Phys.*, *118*(5), 2452–2465. https://doi.org/10.1002/jgra.50265

Luan, X. L., and Solomon, S. C. (2008). Meridional winds derived from cosmic radio occultation measurements. *J. Geophys. Res.*: *Space Phys.*, *113*(A8), A08302. https://doi.org/10.1029/2008ja013089

Mathew, T. J., Nayar, S. R. P., Ravindran, S., and Pant, T. (2010). Characteristics of the equatorial F-region vertical plasma drift observed during post-sunset and pre-sunrise hours. *Adv. Space Res.*, *46*(5), 618–625. https://doi.org/10.1016/j.asr.2010.04.023

Prabhakaran Nayar, S. R., Mathew, T. J., Sreehari, C. V., Sumod, S. G., Devasia, C. V., Ravindran, S., Sreeja, V., Kumar Pant, T., and Sridharan, R. (2009). Electrodynamics of the equatorial F-region ionosphere during pre-sunrise period. *Ann. Geophys.*, *27*(1), 107–111. https://doi.org/10.5194/angeo-27-107-2009

Richards, P. G. (2001). Seasonal and solar cycle variations of the ionospheric peak electron density: comparison of measurement and models. *J. Geophys. Res.*: *Space Phys.*, *106*(A7), 12803–12819. https://doi.org/10.1029/2000JA000365

Richmond, A. D., Ridley, E. C., and Roble, R. G. (1992). A thermosphere/ionosphere general circulation model with coupled electrodynamics. *Geophys. Res. Lett.*, *19*(6), 601–604. https://doi.org/10.1029/92GL00401

Richmond, A. D. (1995a). Ionospheric electrodynamics. In H. Volland (Ed.), *Handbook of Atmospheric Electrodynamics* (pp. 249-290). Boca Raton: CRC Press.

Richmond, A. D. (1995b). Ionospheric electrodynamics using magnetic apex coordinates. *J. Geomagn. Geoelectr.*, *47*(2), 191–212. https://doi.org/10.5636/jgg.47.191

Richmond, A. D., and Maute, A. (2014). Ionospheric electrodynamics modeling. In J. Huba, et al. (Eds.), *Modeling the Ionosphere-Thermosphere System* (pp. 57-71). AGU Geophysical Monograph Series (Vol. 201). Chichester, UK: John Wiley & Sons, Ltd. https://doi.org/10.1002/9781118704417.ch6

Rishbeth, H., and Garriott, O. K. (1969). *Introduction to Ionospheric Physics*. New York: Academic Press.

Roble, R. G., Ridley, E. C., Richmond, A. D., and Dickinson, R. E. (1988). A coupled thermosphere/ionosphere general circulation model. *Geophys. Res. Lett.*, *15*(12), 1325–1328. https://doi.org/10.1029/GL015i012p01325

Wright, J. W. (1962). Dependence of the ionospheric *F* region on the solar cycle. *Nature*, *194*(4827), 461–462. https://doi.org/10.1038/194461a0

Zhang, R. L., Liu, L. B., Chen, Y. D., and Le, H. J. (2015). The dawn enhancement of the equatorial ionospheric vertical plasma drift. *J. Geophys. Res.*: *Space Phys.*, *120*(12), 10688–10697. https://doi.org/10.1002/2015ja021972

Zhang, R. L., Liu, L. B., Le, H. J., and Chen, Y. D. (2016). Evidence and effects of the sunrise enhancement of the equatorial vertical plasma drift in the *F* region ionosphere. *J. Geophys. Res.*: *Space Phys.*, *121*(5), 4826–4834. https://doi.org/10.1002/2016ja022491

Zhou, X., Liu, H. L., Lu, X., Zhang, R. L., Maute, A., Wu, H. N., Yue, X. N., and Wan, W. X. (2020). Quiet-time day-to-day variability of equatorial vertical $\mathbf{E}\times\mathbf{B}$ drift from atmosphere perturbations at dawn. *J. Geophys. Res.*: *Space Phys.*, *125*(4), e2020JA027824. https://doi.org/10.1029/2020ja027824